Bulk Nanocrystalline Aluminum 5083 Alloy Fabricated by a Novel Technique: Cryomilling and Spark Plasma Sintering

JICHUN YE, LEONARDO AJDELSZTAJN, and JULIE M. SCHOENUNG

Dense, bulk nanocrystalline aluminum 5083 alloy was fabricated *via* a combined technique: cryomilling (mechanical milling at cryogenic temperature) to achieve the nanocrystalline Al 5083 powder and spark plasma sintering (SPS) to consolidate the cryomilled powder. The results of X-ray diffraction analysis indicate that the average grain size in the SPS consolidated material is 51 nm, one of the smallest grain sizes ever reported in bulk Al alloys produced by powder metallurgy derived methods. In contrast, transmission electron microscopy (TEM) analysis revealed a bimodal grain size distribution, with an average grain size of 47 nm in the fine-grained regions and approximately 300 nm in the coarse-grained regions. Nanoindentation was used to evaluate the mechanical properties and the uniformity of the consolidated nanocrystalline Al 5083. The hardness of the material is greatly improved over that of the conventional equivalent, due to the fine grain size. The mechanisms for spark plasma sintering and the microstructural evolution are discussed on the basis of the experimental findings.

I. INTRODUCTION

AT present, there are only a limited number of fabrication methods that can be used to synthesize bulk nanocrystalline metals[1,2] that have sufficiently large dimensions for practical applications. Powder metallurgy–based consolidation methods, which can be used for this purpose, normally involve the synthesis of nanocrystalline powder and subsequent consolidation.[3] Nanocrystalline powder can be produced by numerous processing methods, such as mechanical milling, evaporation condensation, and precursor decomposition.[2,3] Mechanical milling, especially cryomilling, is an effective approach to synthesize a large quantity of nanocrystalline metallic powder.

Cryomilling is normally conducted in a liquid nitrogen atmosphere, suppressing the dynamic recovery and recrystallization by the cryogenic temperature and thus facilitating grain refinement in metallic powder.[4] Cryomilling can be easily scaled up and has the potential to be economically feasible.[5] Koch[6] pointed out that two problems may occur with cryomilling: (1) the contamination from the milling media and atmosphere and (2) grain coarsening during powder consolidation. It has been demonstrated, however, that the contamination introduces impurities (*e.g.*, Fe) and *in-situ* formed compounds (*e.g.*, nitrides and oxides) that are approximately 2 to 10 nm in size and are uniformly dispersed in the cryomilled powder, resulting in greatly improved thermal stability[7] and mechanical properties.[8] In contrast, severe grain growth has been observed at room temperature in nanocrystalline Al that is free of such impurities, because it was synthesized with a chemical method.[9]

Conventional consolidation of cryomilled powder can, however, lead to significant grain growth. For example, an average grain size of 116 nm was observed in a hot isostatically pressed (''hipped'') Al-Mg alloy,[10] and the grain size in a 5083 Al consolidated by cold isostatic pressing (CIP) and extrusion was 207 nm.[11] The bulk materials will exhibit unique properties only if the initial nanocrystalline structure in the powder is preserved after the consolidation process. Spark plasma sintering (SPS), a relatively new sintering technique, has been demonstrated to successfully consolidate nanosized powder into a dense bulk material in a shorter time and at lower temperatures than would be required with conventional consolidation methods, both of which facilitate the retention of the fine structure in the starting materials.[12]

Spark plasma sintering is a modified hot pressing technique in which pulsed DC current and uniaxial pressure are applied simultaneously. The pulsed current passes through the electrically conductive graphite die and sample, if conductive. Heating of a dielectric sample can be realized through the heat transfer from the die and punches, which are heated by the pulsed current; for a conductive sample, besides the heat transfer, heating also results from the pulsed current due to the Joule effect. This heating style leads to a rapid heating rate (up to 1000 °C/min), making SPS a fast consolidation method.[13,14,15] High current density at the contact points can be formed due to the small contact area at the initial stage of sintering, resulting in a locally high temperature. This locally high temperature can further facilitate the densification. At the initial stage of sintering, electric/spark discharge is generated across the gaps between particles, which promotes the elimination of surface adsorbents or the breakup of oxide layers and, eventually, facilitates the sintering process.[13,16–18]

Recently, nanocrystalline powders have been consolidated using SPS. Various nanocrystalline intermetallic powders, which were synthesized with mechanical milling, have been successfully consolidated into dense materials by SPS within minutes without severe grain growth.[19–26] However, limited research has been conducted on the use of SPS for low melting metals, such as aluminum alloys, especially on nanocrystalline Al alloys. Furthermore, although SPS has been widely applied to consolidate a variety of materials, the densification mechanisms involved in SPS still remain unclear. Due to the specific structural characteristic of the cryomilled powder, *i.e.*, a physical particle containing numerous nanocrystalline grains, it can shed light on the sintering mechanisms.

JICHUN YE, Graduate Student, LEONARDO AJDELSZTAJN, Research Scientist, and JULIE M. SCHOENUNG, Associate Professor, are with the Department of Chemical Engineering and Materials Science, University of California, Davis, CA 95616-5294.

Manuscript submitted November 5, 2005.

In the current study, SPS was used to consolidate a cryomilled nanocrystalline Al alloy powder to achieve dense bulk nanocrystalline material. The microstructures of the powder and the bulk sample were revealed through X-ray diffraction (XRD), transmission electron microscopy (TEM), scanning electron microscopy (SEM), and optical microscopy. The mechanical behavior of the bulk sample was characterized with nanoindentation and microhardness testing. The sintering mechanisms and current effect are explored on the basis of the microstructural studies and analytical calculations.

II. EXPERIMENTAL PROCEDURE

One kilogram of commercial, gas-atomized 5083 Al (4.4Mg, 0.7Mn, 0.15Cr, and the balance Al (wt pct)) powder was cryomilled using a modified Union Process 01-ST attritor (Union Process, Akron, OH) with a ball (6 mm in diameter, stainless steel)–to–powder ratio of 32:1 for 8 hours under a liquid nitrogen environment at a rotation speed of 180 rpm. The 5083 Al alloy was selected for this study because of its widespread application in structural components exposed to marine environments, which require good corrosion resistance. For simplicity, the material will hereafter be referred to simply as Al, even though it is actually an alloy. Two grams of milled powder were placed in a cylindrical graphite die with punches on both ends to seal the die. The powder in the die was cold pressed through the punches under a load of 908 kg for 1 minute. The pressed powder was consolidated using an SPS apparatus (Sumitomo, model 1050, Sumitomo Heavy Industries, Niihama, Japan) under vacuum. The temperature was measured using a K-type thermocouple inserted into a hole located in the center of the die close to the sample. The time to ramp up from room temperature to 350 °C was 180 seconds (1.8 °C/sec), and the sample was kept at that temperature for 120 seconds. The sintering was assisted with uniaxial pressure (80 MPa). The current, temperature, displacement, and displacement rate as functions of time were recorded by the components attached to the SPS apparatus, as shown in Figure 1.

The SPS-consolidated specimen was 20 mm in diameter and 2 mm in thickness. After polishing the sample surfaces, density measurements were made using the Archimedes method of water displacement. X-ray diffraction was performed using a SCINTAG* XDS 2000 powder diffractometer using Cu K_α ($\lambda = 0.1542$ nm) radiation. Background subtraction, $K_{\alpha 2}$ stripping, and calculation of full-width at half-maximum (FWHM) were carried out *via* the software included with the diffractometer. Five diffraction peaks were used to determine the grain size through the calculation of the peak broadening using linear fitting.[27] The morphology of the cryomilled powder was investigated with SEM. Transmission electron microscopy was used to reveal the microstructure and to determine the grain size and grain size distribution for both the cryomilled powder and the consolidated aluminum alloy, using a PHILIPS** CM-12 microscope. High resolution TEM was conducted using an FEI Tecnai F20 electron microscope. In order to achieve a large observable thin area, the TEM samples were prepared using the following procedure. Cryomilled powder and the disk from the SPS-consolidated specimen were ground and then dimpled down to approximately 15 μm in thickness. The final thinning perforation process was conducted using argon ion milling with an angle range from 22 to 10 deg. The sample temperature was kept at 20 ± 5 °C during ion milling. Optical microscopy was utilized to distinguish the coarse-grained region from the fine-grained region, either with or without the treatment of Keller's reagent (2.5 mL HNO_3, 1.5 mL HCl, 1 mL HF, 95 mL H_2O). Nanoindentation (MTS Nanoindenter XP Berkovich indenter) was used to evaluate the mechanical properties and the uniformity of the consolidated material. Microhardness was also used to obtain the hardness value in HV units for direct comparison with that of the conventional equivalent.

*SCINTAG is a trademark of Scintag Inc., Cupertino, CA.

**PHILIPS is a trademark of Philips Electronic Instruments, Mahwah, NJ.

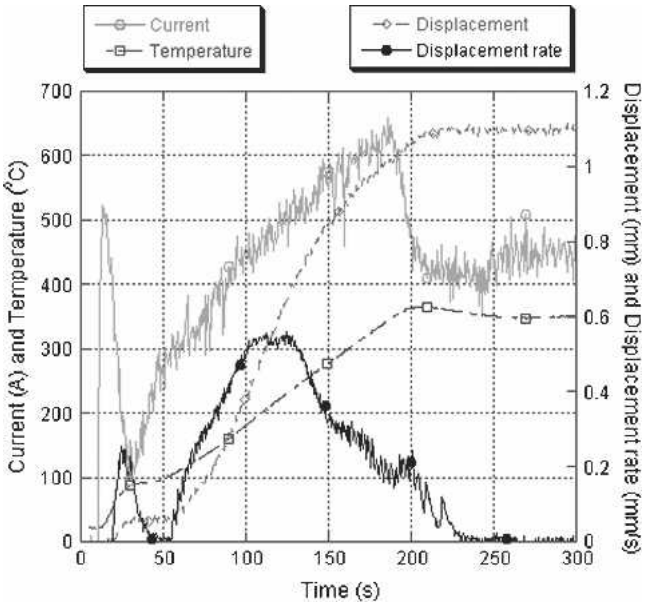

Fig. 1—Evolution of current, temperature, displacement, and displacement rate of the cryomilled 5083 Al powder during SPS.

III. RESULTS

A. *Cryomilled Powder*

Figure 2 shows the as-cryomilled powder having an equiaxed shape and a particle size of 10 to 50 μm, which results from repeated fracturing and cold welding involved in the mechanical milling.[4,6] The milled metallic particles are not dense, but featured with crevices and pores. The cryomilled powder particle consists of numerous nanocrystalline grains in the size range of 25 nm, as determined from the investigation of XRD peak broadening.[27] The correlation coefficient of the linear fit for the grain size calculation was 0.98. The nanostructure of the cryomilled powder was verified with a bright-field TEM image, as shown in Figure 3(a). The typical nanocrystalline Al grains are equiaxed and randomly distributed. The selected-area diffraction (SAD) pattern shows continuous rings, which is a typical diffraction pattern for nanocrystalline materials. Figure 3(b) displays the grain size distribution of the cryomilled Al

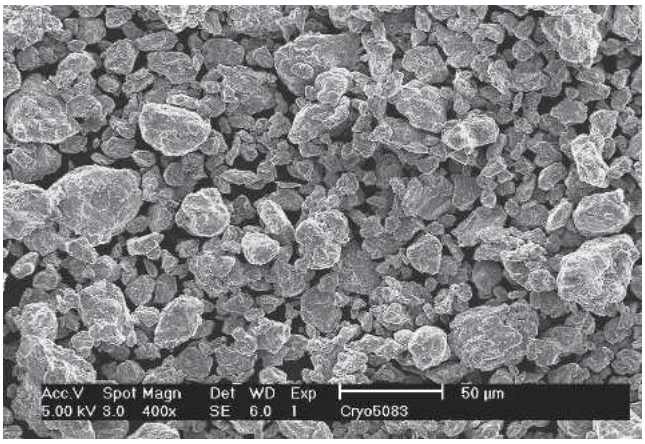

Fig. 2—Secondary electron SEM image showing the morphology and size of the cryomilled 5083 Al powder.

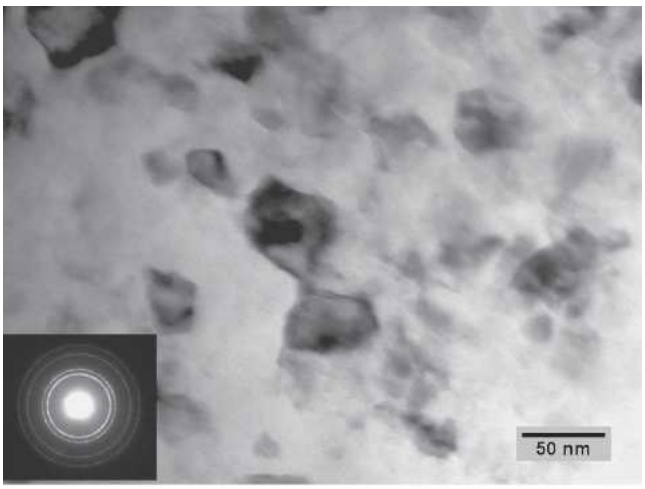

(*a*)

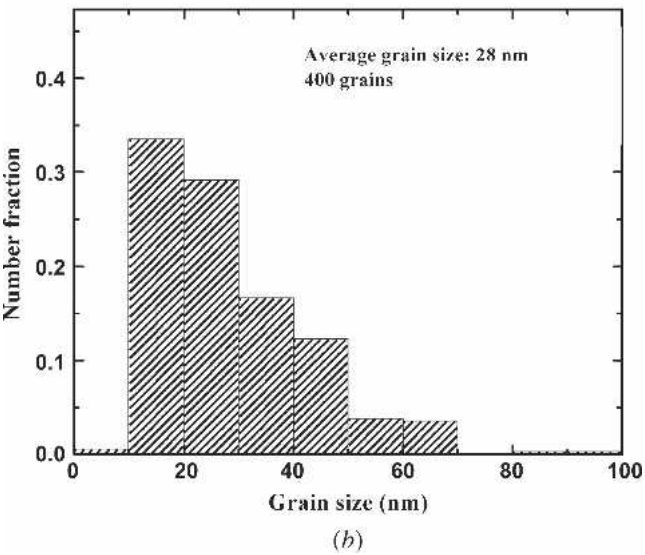

(*b*)

Fig. 3—TEM results for the cryomilled 5083 Al: (*a*) representative bright-field image and SAD pattern; and (*b*) distribution histogram of the Al grain size as determined from the TEM images.

powder (determined from 400 grains measured). The size range of the grains is 10 to 70 nm, more frequently 10 to 40 nm, with the average size at 28 nm, which is consistent with the result from the XRD measurement.

B. *The Bulk SPS-Consolidated Material*

The cryomilled Al powder was consolidated by SPS to produce a disk-shaped specimen, hereafter referred to simply as the bulk sample. A near fully dense bulk Al (99.0 ± 0.1 pct of theoretical density) was achieved by SPS. The XRD spectra for both the bulk sample and the cryomilled powder are presented in Figure 4. Only Al peaks are observed in the spectra. It is noticeable that the broadening of the peaks is smaller after SPS, indicating that grain growth or microstrain release occurred during SPS. The average grain size in the bulk sample was 51 nm, as determined by peak broadening, which is one of the smallest grain sizes for bulk nanocrystalline Al alloys ever reported.

A bimodal grain size distribution was observed from the TEM study. This bimodal grain size distribution can actually be desirable because it can enhance the mechanical properties of the bulk material, with the fine grains contributing to the strength and the coarse grains contributing to the ductility.[11] Figure 5(a) is a bright-field TEM image, showing the microstructure of the Al in the fine-grained region. The appearance of the grains is equiaxed, resembling that in the as-cryomilled powder. The grain size distribution in the fine-grained region in the bulk sample is shown in Figure 5(b). Most of the grains are within the size range of 20 to 60 nm, with an average size of 47 nm (determined by measuring 990 individual grains). The profile of the grain size histogram for the fine grains in the bulk sample is similar to that for the as-cryomilled powder, except that the columns shift to the right by approximately 20 nm. This increase in grain size observed in the bulk sample is attributed to the grain growth during SPS, where the material experienced a high temperature (350 °C, 0.72 T_m) for a few minutes. Some isolated large grains larger than 100 nm in size are present in the fine-grained region (Figure 5(a)), a consequence of locally heterogeneous grain

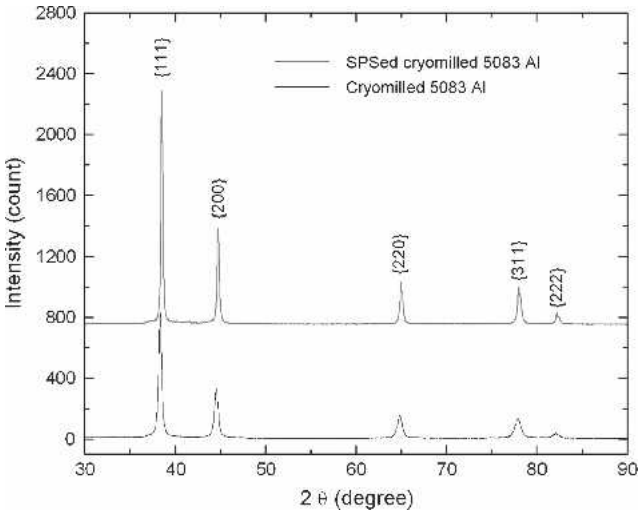

Fig. 4—XRD spectra of cryomilled 5083 Al powder and the SPS-consolidated cryomilled 5083 Al. Only Al peaks are observed.

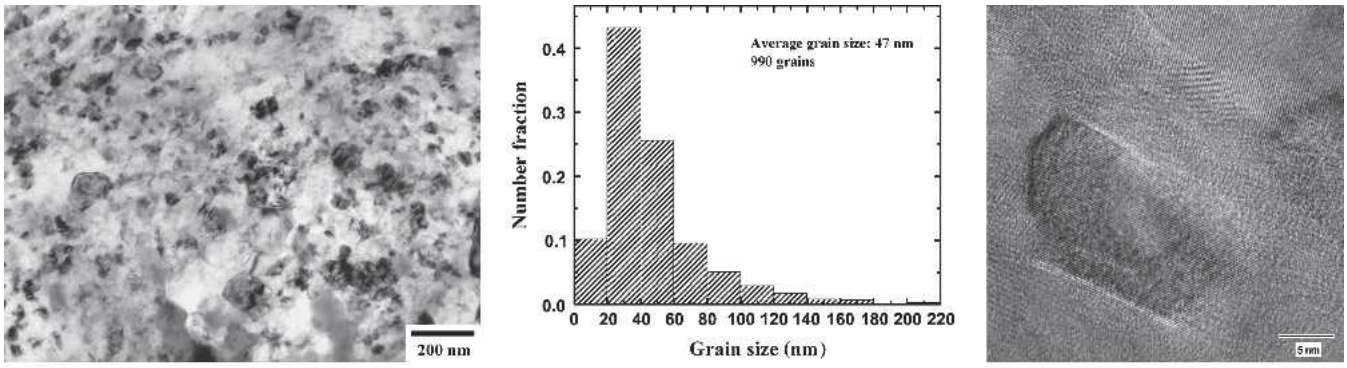

Fig. 5—TEM results from the fine-grained region in the SPS-consolidated cryomilled 5083 Al: (*a*) representative bright-field image, (*b*) distribution histogram of the Al grain size as determined from the TEM images, and (*c*) high-resolution TEM image, showing a very fine grain.

growth. A very fine grain 20 nm in size is observed with high-resolution TEM (Figure 5(c)).

Aggregates of coarse grains are also frequently observed in the bulk sample. The coarse-grained aggregates, with the dimension of a few microns, are surrounded by the nanocrystalline Al, as illustrated in Figures 6 and 7. Figure 6(a) is a bright-field TEM image, showing the coarse-grained aggregates (in the middle) and the nanocrystalline Al regions (on the top and bottom). Figure 6(b) is a corresponding dark-field TEM image. A rectangular grain approximately 0.8 μm in size is observed in both the bright- and dark-field images at the left corner in the coarse-grained aggregate. A large grain, 1.5 μm in size, which is indiscernible in the bright-field image, reveals its true features in the dark-field image. Both of these coarse grains are equiaxed, which suggests that this coarse-grained aggregate was likely formed through melting and crystallization. It is also possible, however, that the coarse-grained aggregate was formed by severe grain growth. The inset in Figure 6(a) is a diffraction pattern, with the ring pattern for the nanocrystalline Al and the spot pattern for the coarse-grained Al. Another interesting coarse-grained structure is shown in Figures 6(c) and (d). A large grain, approximately 2 μm in size, is discernible in both the bright- and dark-field images. This grain has an irregular shape, with a somewhat smaller rectangular protrusion on the edge of a large rectangular grain. The inset in Figure 6(c) is a diffraction pattern from the large grain, a typical diffraction pattern for single-crystal fcc metals.

A series of band structures with widths 30 to 200 nm in size are observed in the bulk sample, as shown in Figure 7(a). These band structures (or lamellar structures) are consistent with a recrystallized microstructure.[28,29] In addition to these band structures are the randomly orientated fine grains. It should be noted that, in the current study, this type of band structure is less frequently observed than the coarse-grained aggregates in the bulk sample during TEM examination, and that it can be present in regions other than the outer surfaces of the particles. Figure 7(b) shows a fine-grained region within the bulk sample that contains two coarse-grained regions, as indicated by A and B. In region A (approximately 2 μm in length), several well-defined coarse grains are observed. In region B, an irregularly shaped coarse grain is seen. These regions were likely formed by diffusion of atoms to the pores and crevices in the cryomilled powders; however, localized abnormal grain growth is also a possibility.[30]

Although it is more likely that the coarse-grained aggregates formed on the outer surface of the cryomilled powder due to the higher temperature on the surface, there is a lack of direct evidence from the TEM investigation to support this claim. Optical microscopy, however, provided further insight. Figure 8(a) shows an optical micrograph of a well-polished surface of the bulk sample. The bright regions correspond to the coarse-grained Al, and the dark regions represent the fine-grained Al. The volume fraction of the bright region is about 10 pct, as determined with the software ANALYSIS.* Although the distribution of the coarse grains (bright) is not uniform, it can be seen that the fine-grained regions are surrounded by the coarse grains, indicating that the coarse-grained aggregates are most often formed on the outer surfaces of the cryomilled powder, whereas the inner region of the powder retains the fine-grained structure. A similar microstructure has been observed in a nanocrystalline Fe-23Al-6C materials synthesized by mechanical milling and SPS.[19] Figure 8(b) is an optical micrograph showing the bulk sample after etching with Keller's reagent. The shape of the powder particles, which is closely packed and resembles that of the as-cryomilled powder, is clearly delineated with the reagent. The dimension of the dark regions in Figure 8(a) and the size of the delineated particles in Figure 8(b) are consistent with the dimension of the cryomilled powder particles, as shown in Figure 2. Within the dark fine-grained particles observed in Figure 8(a), there are small bright regions. These represent regions within the cryomilled particles where grain growth has occurred, potentially as the result of local recrystallization or diffusion into the pores and crevices of the cryomilled powder.

It should be noted that when using XRD analysis to determine average grain size, any diffraction peak line broadening that results from crystallites with grain sizes in excess of 100 to 300 nm is considered to be negligibly small.[31] This implies that the coarse grains formed

*ANALYSIS is a trademark of Olympus Soft Imaging Solutions Corp., Lakewood, CO.

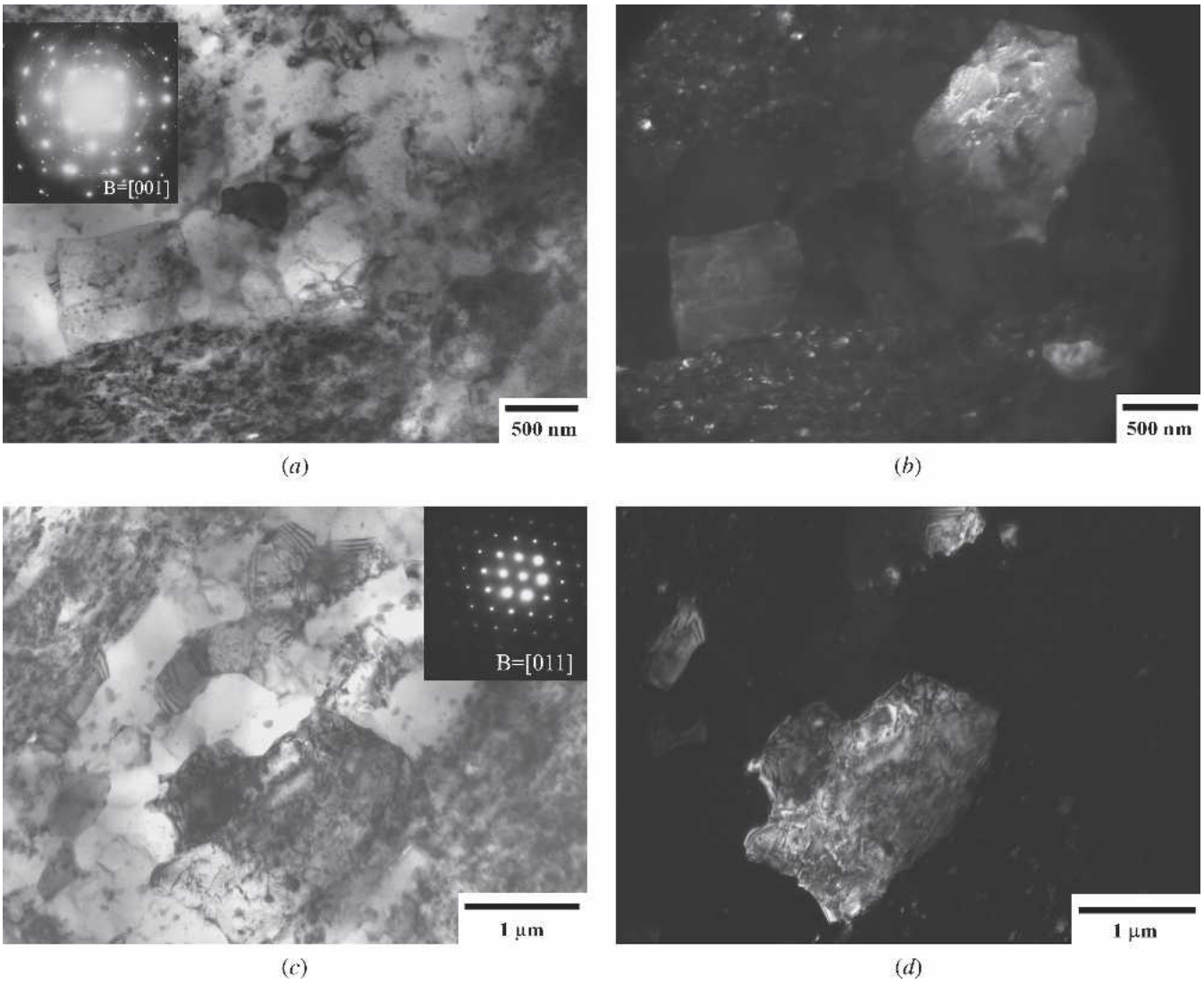

Fig. 6—TEM images from SPS-consolidated cryomilled 5083 Al showing both the coarse-grained regions and fine-grained regions: (*a*) first bright-field image; (*b*) corresponding dark-field image of (a); (*c*) second bright-field image and SAD pattern; and (*d*) corresponding dark-field image of (*c*).

during SPS make an insignificant contribution to the peak broadening. The grain size value of 51 nm determined from XRD analysis is the volume-averaged value from those grains with sizes less than 100 nm. This value for the average grain size is consistent with that in the fine-grained regions, as determined by TEM (47 nm).

C. *Mechanical Properties*

Nanoindentation tests were performed on the bulk sample with an indentation depth of 500 nm. The continuous stiffness measurement (CSM) approach was used to determine the hardness values from the nanoindentation tests.[32] Two different directions were chosen to evaluate the mechanical response of the specimen (shown in the inset of Figure 9): (1) radially from the center of the disk-shaped sample to the edge (along line OA) and (2) along its thickness (along line OB).

The nanoindentation results (Figure 9) indicate that the average hardness shows minimal variation from the center to the edge and from the top to the bottom (thickness) of the bulk sample. Nevertheless, one can observe that microscopically the hardness varies slightly from point to point, implying that there is a variation, but not a gradient, in microstructure. This observation is confirmed by the microscopy analysis where the different microstructural features are present in the bulk sample. The hardness was also evaluated with a microhardness tester for a direct comparison with conventional Al 5083. The hardness of the bulk material prepared by SPS is 165 $\pm$ 6 HV, which is almost twice the value for conventional Al 5083.[33] This significant improvement in hardness of the bulk nanocrystalline SPS-consolidated material can be attributed to its fine grain structure.

IV. DISCUSSION

A. *Grain Growth in the Fine-Grained Region*

As determined through image analysis, the SPS-consolidated cryomilled Al 5083 is observed to be comprised

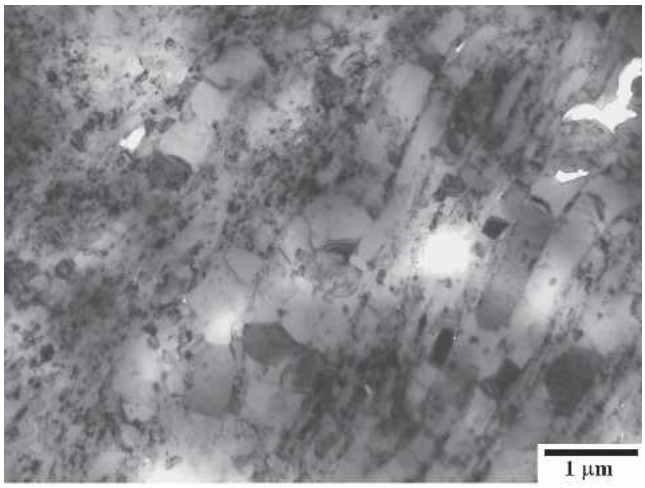

(*a*)

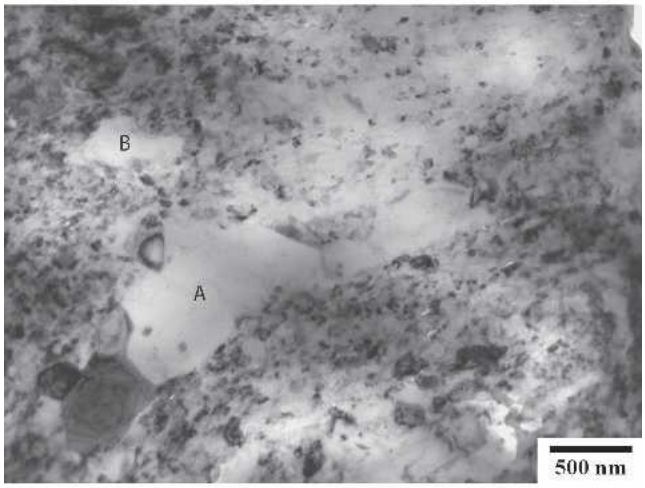

(*b*)

Fig. 7—TEM bright-field images from SPS-consolidated cryomilled 5083 Al showing (*a*) the band structure and (*b*) separated narrow coarse-grained aggregates (as indicated by regions A and B in the SPS-consolidated cryomilled 5083 Al).

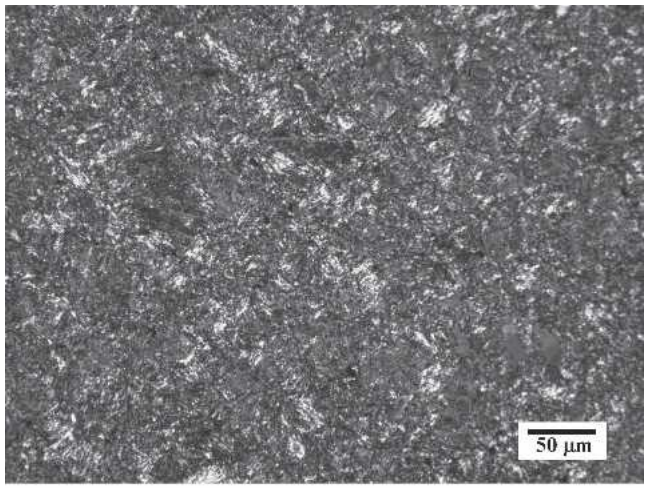

(*a*)

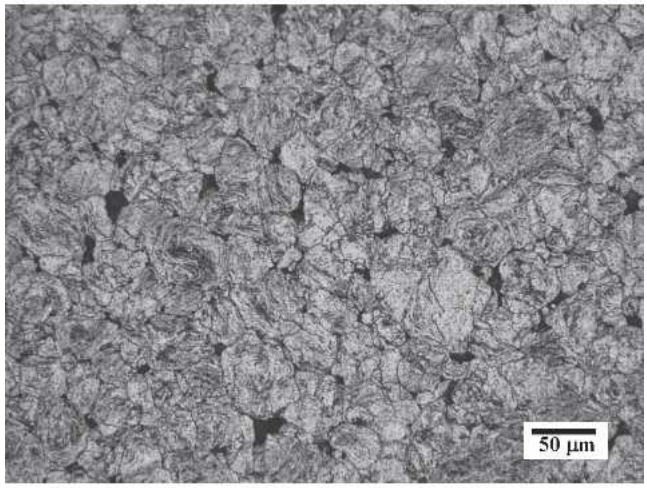

(*b*)

Fig. 8—Optical micrographs of the SPS-consolidated cryomilled 5083 Al: (*a*) well-polished surface, showing the coarse-grained aggregates (bright regions) and fine-grained regions (dark regions); and (*b*) etched surface showing the contour of the particles.

of approximately 90 pct fine grains with an average size of 47 nm and 10 pct coarse grains with an average grain size of 300 nm. The average grain size in the fine-grained region is approximately 20 nm larger than that observed in the cryomilled Al powder prior to consolidation (25 nm). The kinetics of grain growth in conventional polycrystalline materials is normally controlled by atomic diffusion at the grain boundaries and can be expressed as[7,34]

$$d^{1/n} - d_0^{1/n} = kt \qquad [1]$$

where d is the grain size at time t, d_0 is the initial grain size, k is the temperature-dependent rate constant, and n is the grain growth exponent. A systematic study of isothermal annealing on the grain growth behavior of cryomilled Al powder, which was cryomilled using the same milling parameters as those used in this study, was conducted by Zhou *et al.*[7] In their study, the grain size *vs* time data were fitted mathematically to Eq. [1] to determine the parameters of k and n. The grain growth exponent in Eq. [1] was approximately 0.05 for temperatures lower than 0.78 T_m, where T_m is the absolute melting temperature. The fitted values of k were plotted *vs* 10^4/(RT) to achieve the activation energy for grain growth, shown as Figure 8 in Reference 7 based on a well-known Arrhenius-type equation:

$$k = k_0 \exp(-Q_{gg}/\mathrm{RT}) \qquad [2]$$

where k_0 is the rate constant independent of the absolute temperature T, Q_{gg} is the activation energy for grain growth, and R is the molar gas constant. The activation energy for grain growth was determined to be 79 kJ/mol.[7]

In the current study, the highest temperature involved in the SPS consolidation was 350 °C (0.72 T_m), which is less than 0.78 T_m. Therefore, the exponent value n can be treated as 0.05 for all the temperatures, and Eq. [1] becomes $d^{20} - d_0^{20} = kt$. Although most of the grain growth will probably occur at high temperatures (~350 °C), the grain

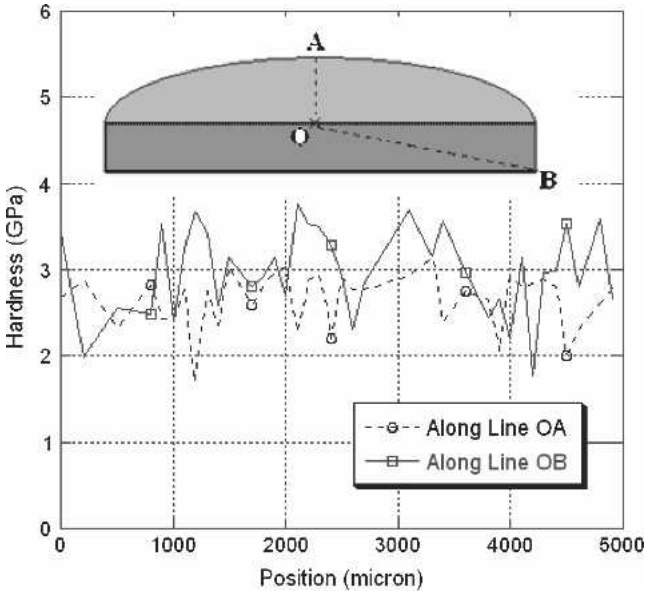

Fig. 9—The corresponding hardness values derived from nanoindentation for SPS-consolidated cryomilled 5083 Al. The inset is the schematic showing the lines along which hardness was measured using nanoindentation.

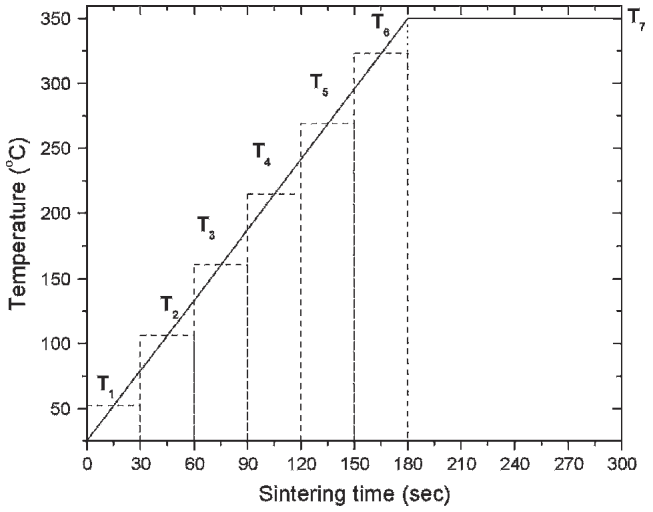

Fig. 10—Schematic showing the constituent elements used to approximate the temperature during SPS for the grain growth estimation.

growth cannot be neglected during the heating stage from room temperature to 350 °C. As an approximation, the linear heating can be divided into six constituent elements plus a holding stage as the seventh element, with the mean temperature designated as T_j ($j = 1, 2, \ldots, 7$), as shown in Figure 10. Equation [1] is applied to each stage, yielding the following formulas:

$$d_1^{20} - d_0^{20} = k_1 t_1$$
$$\ldots$$
$$d_7^{20} - d_6^{20} = k_7 (t_7 - t_6)$$

where t_j and d_j are the time and grain size, respectively, at the end of each stage.

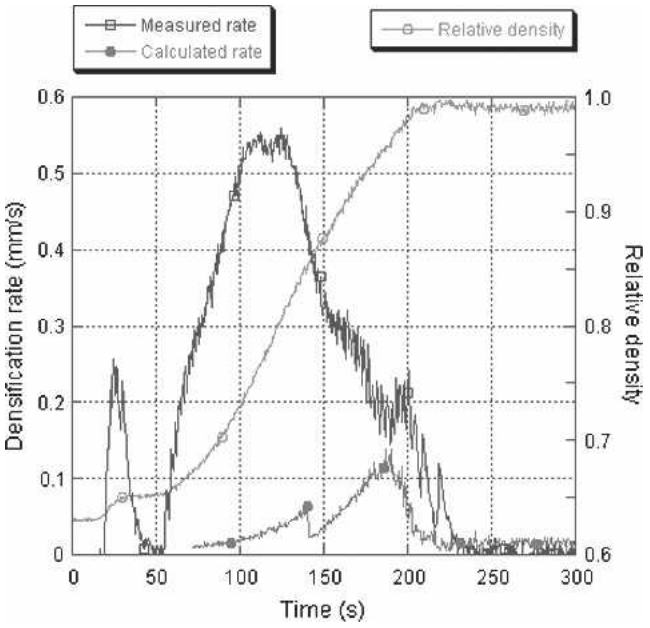

Fig. 11—The relative density and the measured and the calculated densification rates as a function of time during the SPS consolidation of cryomilled 5083 Al.

These equations are summed and values for t_j are substituted, giving rise to

$$d_7^{20} - d_0^{20} = 30(k_1 + k_2 + k_3 + k_4 + k_5 + k_6) + 120k_7 \quad [3]$$

where k_j is the rate constant at the temperature of T_j, which can be obtained from Figure 8 in Reference 7 after modification with a constant for unit conversion, assuming the activation energy for grain growth is taken as 79 kJ/mol, the value deduced for the cryomilled Al. Since the material used in this study is 5083 Al, which is slightly different than the material (pure Al) used in Reference 7, the k_j values were obtained on the basis of T_m. When $1/n = 20$, $d_7^{20} \gg d_0^{20}$ and Eq. [3] can be simplified to

$$d_7^{20} = 30(k_1 + k_2 + k_3 + k_4 + k_5 + k_6) + 120k_7 \quad [4]$$

As a result, the final grain size (d_7^{20}) after 180 seconds of ramping and 120 seconds of holding at 350 °C is calculated to be 39 nm, which is less than the values determined from both TEM and XRD, indicating that the real activation energy for grain growth during SPS is slightly lower than that for isothermal annealing, yielding a higher grain growth rate.

It is believed that the current through the specimen can enhance the mass transport rate during SPS.[13,16] Garay *et al.* examined the current effect on the growth rate for intermetallic materials in the Ni-Ti system and found it to be enhanced by 43 times at a current density of 2546 A/cm^2 when compared to that without current at a constant temperature of 650 °C.[14] In another related study, Lormad *et al.* observed significant grain growth in several metals when under the influence of an electric current. Furthermore, the direction of motion of these grain boundaries was biased (*i.e.*, preferential migration toward the

electrode).[35] The limited effect of the current on the grain growth in the inner part of the cryomilled particle, as observed in the current study, which is manifested either by limited grain growth or equiaxed grains in the fine-grained region, indicates that the current density in the inner part of the cryomilled Al particle is very small, even though it is an electrically conductive material.

In this study, a load of 80 MPa was used to assist the densification during SPS. In conventional sintering, the applied load not only facilitates the densification but also enhances the grain growth rate. In a related study by Park *et al.*,[10] the average grain size of cryomilled Al evolves from 25 to 116 nm after hot isostatic pressing (HIP) at 350 °C for 10,800 seconds with the assistance of an isostatic pressure of 170 MPa. As a comparison, in an isothermal annealing study, the cryomilled Al only grew to a size of 50 nm after the same time at the same exposure temperature.[7] It is apparent that the pressure has a significant influence on the grain growth, due to the enhanced diffusivity under the applied pressure. In the current study, the Al grains in the inner part of the particle remain very fine (47 nm), even with the assistance of the current and pressure. This result indicates that both the current and the load have little effect on the grain growth in the inner part of the particle. The insignificant effect of current has been discussed previously, and the negligible effect of the load is explained subsequently. Because the temperature on the outer surface of the particle is very high and may exceed the melting point of the Al in localized regions, the outer surface becomes softer either by the softening at higher temperature or by the melting to liquid phase. The applied load is damped by the softer surface, and the actual strain in the inner part of the particle introduced by the load is alleviated, resulting in an insignificant effect of load on the grain growth.

Although 10 pct of the grains are coarse grains, the overall grain size in the SPS-consolidated cryomilled 5083 Al is still small, one of the smallest grain sizes ever reported in bulk Al alloys produced by powder metallurgy derived methods. For example, an average grain size of 116 nm has been observed in a hipped Al-Mg alloy,[10] while the grain size in a 5083 Al consolidated *via* CIP and extrusion was 207 nm.[11] This smaller grain size is attributable primarily to the short sintering time needed for SPS consolidation.

B. *Origin of the Coarse Grains*

The coarse grains observed in this study actually are not the traditionally defined coarse grains, which would be on the order of 1 μm or larger in size, but instead are in the submicron range, which is coarse in comparison to the fine-grained regions. The origin of the coarse grains is explored on the basis of experimental observations and several mechanisms are proposed, as discussed subsequently. As discussed earlier, the current effect during SPS consolidation is insignificant in the inner part of the Al particle. This implies that most of the current is distributed on the outer surface of the particle, *i.e.*, the current density on the outer surface is very high. As a fundamental physical phenomenon, at high frequency, current is normally confined to the outer surface or skin of a conductor, which is known as the *skin effect*.[36] The current density decreases exponentially from the outer surface to the interior region.[36] Moreover, during the initial stage of SPS consolidation when the particle contact area is small, the local current density is even higher. The high current density at these surface contact points results in extremely high temperature due to Joule heating, which leads to melting or severe grain growth at these regions. The SPS has been used successfully to weld metals and metal matrix composites, providing further evidence of the local melting or rapid mass transport on the surface.[37]

Minamino *et al.* attributed the coarse-grained region observed in their work on the outer surface of mechanically milled Fe-Al-C to a molten layer.[23] On the other hand, Koizumi *et al.* proposed that the formation of the coarse-grained region that surrounds the fine-grained region is due to severe grain growth.[19] In the case where the local temperature is high enough to produce a molten layer, the temperature of the solid phase adjoining this molten layer is also very high. At such a high temperature, also with the assistance of the high current density and applied pressure, severe grain growth is expected on the outer surface. Therefore, melting and severe solid-state grain growth can both be responsible for the formation of the coarse-grained aggregates on the outer surface of the SPS-consolidated particles.

Hu[38] proposed that grains/subgrains might rotate by a boundary diffusion process until adjacent grains were of similar orientation. These grains would then coalesce into a larger grain. Zhou *et al.* applied this mechanism to explain the grain growth in cryomilled Al powder.[29] The large grains can ''eat'' NC Al grains, or NC Al grains coalesce with each other to form medium-sized grains and then these medium-sized grains coalesce to form large grains. However, direct evidence is still lacking to support this mechanism for grain growth. In the current study, a coarse grain with a relatively smaller rectangular protrusion on an edge of the large rectangular grain is observed, which is not stable thermodynamically, as shown in Figures 6(c) and (d). This structure provides direct experimental proof of grain coalescence as a possible grain growth mechanism.

A band structure is observed in the SPS-consolidated cryomilled 5083 Al. This band structure is a typical structure observed in severely deformed metals after annealing (including cryomilled powder).[28,29] Zhou *et al.* found this band structure in cryomilled Al after isothermal annealing at a temperature of 250 °C for 1 hour.[29] Thus, this band structure need not occur only at the outer surface of the particles, because the average temperature in the specimen is approximately 350 °C. Coarse grain aggregates can also be formed by diffusion to fill the interparticle spaces or the pores and crevices of the cryomilled powders, as observed in Figure 7(b).[30] The temperature in the regions around these pores and crevices is also high due to the skin effect of the current. Therefore, the diffusion in these regions is greatly enhanced by the high temperature and high current density, allowing diffusion to result in the filling of these spaces within a few minutes.

C. *Densification Mechanisms*

The densification mechanisms involved in SPS consolidation are still under discussion within the research community. Researchers have attributed the fast densification process in SPS to the interparticle electric discharge and current effect, which also have been discussed in this article

to explain the microstructural features in the bulk sample. However, few quantitative research efforts have been undertaken to investigate the densification mechanisms during the SPS process. Koizumi *et al.* extrapolated the well-established densification theory for the HIP process to the SPS process, and a reasonable match was obtained.[19] As discussed by Koizumi *et al.*,[19] the role of the applied pressure in SPS can be treated as quasi-isostatic pressing, *i.e.*, isostatic in the inner region of the compact but not near the surface. A certain amount of material near the surface is usually removed during polishing, which would probably remove the layer that experienced anisostatic pressing. Furthermore, powder synthesized with mechanical milling normally has a granular shape with good fluidity. It is possible to apply isostatic pressure to most of the powder specimen through granular powders as a pressure-transmitting medium.[39] The densification behavior in HIP has been quantitatively investigated and densification maps have been developed on the basis of the contribution of each mechanism.[40,41,42] In these studies, it was determined that plastic yielding, power-law creep, and diffusion from the particle contact zones to the void surface are the principle densification mechanisms involved in the HIP process. Viscous flow,[42] Nabarro–Herrring and Coble creep,[41] and pore separation and grain growth[41] are some other possible densification mechanisms. The aforementioned mechanisms in HIP are likely to occur in the SPS process, due to the reasonable approximation of the isostatic pressure status in SPS.

Similar to HIP, the densification mechanisms in SPS can be revealed with the study of the dimensional change during SPS. The dimensional change can also be expressed as the change in relative density. The machine itself influences the value of the dimensional change, as a result of the thermal expansion from both the electrodes and graphite punches during the heating stage. Therefore, the dimensional change shown in Figure 1 must be modified to account for this thermal expansion. The evolution in the relative density, being modified for thermal expansion, and the densification rate are plotted and shown in Figure 11. A set of mathematical expressions developed for HIP consolidation are used here in an attempt to explore the densification mechanisms involved in SPS consolidation, as shown subsequently.[40,41,42]

(1) Plastic yielding:

$$\dot{D}_{\text{Yield}} = \infty \text{ if } p > p_{\text{lim}} \quad [5]$$

$$\dot{D}_{\text{Yield}} = 0 \text{ if } p \leq p_{\text{lim}} \quad [6]$$

$$p_{\text{lim}} = 1.3\frac{(D^3 - D_0^3)}{(1 - D_0)}\sigma_y \text{ if } D \leq 0.9 \quad [7]$$

$$p_{\text{lim}} = \frac{2\sigma_y}{3}\ln\left(\frac{1}{1 - D}\right) \text{ if } D > 0.9 \quad [8]$$

where $\dot{D}$ is the densification rate, D is the relative density, D_0 is the initial relative density, σ_y is the yield strength, p is the applied pressure, and p_{lim} is the limiting external pressure required to cause yielding.

(2) Power-law creep (PLC):

$$\dot{D} = 5.3(D^2 D_0)^{1/3}\frac{x}{R}\left(\frac{\dot{\varepsilon}_0}{\sigma_0^n}\right)\left(\frac{P_{\text{eff}}}{3}\right)^n \text{ if } D \leq 0.9 \quad [9]$$

$$\dot{D} = \frac{3}{2}\left(\frac{\dot{\varepsilon}_0}{\sigma_0^n}\right)\frac{D(1 - D)}{[1 - (1 - D)^{1/n}]^n}\left(\frac{3}{2n}P_{\text{eff}}\right)^n \text{ if } D > 0.9 \quad [10]$$

where x is the neck radius, R is the particle radius, $(\dot{\varepsilon}_0, \sigma_0, n)$ are the power-law parameters, and P_{eff} is the effective pressure.

(3) Diffusion from interparticle boundaries:

$$\dot{D} = \frac{43(1 - D_0)^2}{(D - D_0)^2}\frac{(\delta D_b + \rho D_v)}{\text{k}TR^3}\Omega P_{\text{eff}} \text{ if } D \leq 0.9 \quad [11]$$

$$\dot{D} = 54\frac{\Omega(\delta D_b + rD_v)}{\text{k}TR^3}5(1 - D)^{1/2}P_{\text{eff}} \text{ if } D > 0.9 \quad [12]$$

where δD_b is the grain boundary diffusion coefficient times the boundary thickness, D_v is the volume diffusion coefficient, ρ is the radius of curvature of the neck, r is the pore radius, Ω is the atomic volume, k is the Boltzmann constant, and T is the absolute temperature. The yield strength (σ_y), shear modulus (μ) and diffusivity (D_v and δD_b), are temperature-dependent values. The terms P_{eff}, x, r, and ρ are each a function of relative density. These values can be derived from the equations in the Appendix. All of the parameters used for subsequent calculation are also listed in the Appendix.

The value of p_{lim} was calculated from Eqs. [7] and [8]. It is found that when the time is less than 72 seconds, p_{lim} is less than 80 MPa (the applied pressure), indicating that plastic yielding contributed to the densification of the cryomilled Al at this stage. This phenomenon is similar to that in the HIP process, *i.e.*, the plastic yielding is significant during the initial stage and then this effect diminishes and finally disappears as the area of particle contact becomes larger. It is foreseeable that the effect of plastic yielding is more significant in SPS than in HIP, because SPS can provide local regions of high temperature in the specimen, which causes the material to soften. For this reason, the extension of plastic yielding, *i.e.*, after 72 seconds during SPS, is possible. Swinkes *et al.* proposed that viscous flow is a possible densification mechanism in HIP.[42] As discussed previously, during the initial stage of SPS consolidation, temperatures higher than the equilibrium values measured by the thermocouple can occur at localized regions. These elevated temperatures may cause regional melting on the outer surface of the particle, leading to significant viscous flow. The enhanced plastic yielding and viscous flow can be the cause of the first peak in the measured densification rate (Figure 11).

The effects of power-law creep and diffusion were evaluated using Eqs. [9] through [12]. After plastic yielding stops, power-law creep and diffusion begin to dominate as causes of densification. From the time of 73 to 140 seconds, the densification rate associated with power-law creep is 6 to 10 times that of diffusion, indicating that the dominant densification mechanism is the power-law creep. After that period, the densification rates caused by these two mechanisms tend to be equivalent, indicating both power-law creep and diffusion are the main densification mechanisms. The sum of the densification rate from the power-law creep and diffusion as a function of time is plotted in Figure 11 as the ''calculated'' value. There are two noticeable differences between the measured and calculated densification rates. First, the calculated value is much less than the measured, indicating that either other densification mechanisms are involved in SPS at this stage or the densification rates associated with power-law creep and diffusion in SPS are much higher than those in HIP. Helle *et al.*[41] observed that a new densification mechanism (Nabarro–Herring/Coble creep) contributes to densification in HIP, if the grain size is significantly smaller than the particle size. Considering this effect for the current study, the Nabarro–Herring/Coble creep effect is estimated to be one tenth that of the power-law creep, if a grain size of 200 nm is assumed, and is comparable to that of power-law creep, if a grain size of 50 nm is assumed. The grain size on the outer surface is quite large, according to the TEM observations, and thus 200 nm is a more appropriate choice for the calculation. For this situation, the effect from Nabarro–Herring/Coble creep is insignificant. Also, the mechanism of plastic yielding may extend to this stage, but it seems that the enhanced densification rate is more likely attributed to the current effect; *i.e.*, the high current density at the contact regions enhances the mass transport. Garay *et al.*[14] observed a significant increase (~40 times) in the mass transport rate during SPS consolidation. The second difference observed in Figure 11 is that the peak in the measured curve is located left of the peak in the calculated one. Early in the process there is less contact area and thus higher current density, which is not accounted for in the equations derived for HIP consolidation. This higher current density resulted in the higher densification rate (peak) occurring earlier in the process.

D. *Temperature Field Distribution*

For an electrically conductive specimen (such as cryomilled Al), heating can result from both the passing of pulsed current (Joule effect) and the heat transfer from the graphite die and punches.[13] Due to its unconventional heating style, a gradient in the temperature field is possible, and the existence of a temperature gradient then results in a gradient in both microstructure and physical properties within the SPS-consolidated specimen. Wang and Fu[43,44] have measured and calculated the temperature difference between the center of the sample and the inner surface of the die (in the radial direction). If the heating rate is not too high and the specimen is a good thermal conductor, the difference in temperature is small. Otherwise, the temperature at the center could be several hundred degrees centigrade higher than that at the inner surface of the die.[43] Anselmi-Tamburini *et al.*[45] found that the radial temperature difference for a thermally conductive metal (*e.g.*, Cu) is relatively small (~5 °C). Cryomilled Al is a good thermal conductor and the heating rate used in this study is not high; thus, the radial temperature difference should be small (on the order of several degrees centigrade). This small difference caused negligible property variation, as evidenced by the relatively constant average hardness values (Figure 9). In addition to a radial temperature distribution, an axial temperature distribution can exist in SPS. This gradient results from the asymmetric positioning of the plungers in the die.[45] An axial temperature gradient results in inhomogeneity in density and physical properties.[45] In the current study, variations in hardness in the axial direction were not observed. This can be rationalized by the small sample thickness (2 mm) and the good thermal conductivity of the Al.

V. CONCLUSIONS

1. A nanocrystalline 5083 Al alloy powder was fabricated by cryomilling. The cryomilled powder exhibited an equiaxed grain with an average grain size of approximately 25 nm. The particle size of the cryomilled powder was in the range of 10 to 50 μm.
2. The cryomilled powder was consolidated using SPS to a fully dense bulk material at 350 °C in a very short time (300 seconds). The nanostructure in the cryomilled powder was retained after SPS and the average grain size in the SPS-consolidated cryomilled 5083 Al was approximately 50 nm, one of the smallest grain sizes ever reported for bulk Al.
3. During SPS, the current density in the inner part of the cryomilled particles was insignificant, and most of the current was distributed on the outer surfaces of the particles, as determined through the study of the grain growth kinetics in the inner part of the particles and the microstructure of the outer surfaces.
4. Coarse-grained aggregates were observed in the SPS-consolidated cryomilled 5083 Al, most of which were located on the outer surfaces of the particles, as a result of locally high temperature caused by the electric discharge and high current density at these regions. These coarse grains can be formed by melting, severe grain growth, and diffusion.
5. The densification mechanisms involved during SPS were revealed by the study of the microstructure and the densification rate. It seems that plastic yielding, viscous flow, creep, and diffusion are responsible for densification during SPS. Also, the current affected the mass transport during SPS and greatly enhanced the rate of grain growth at the outer surfaces of the particles, as well as the creep and diffusion rates.
6. No hardness gradients were observed in either the radial or axial direction, indicating negligible temperature variations within the SPS die. However, local variations in hardness were observed, providing further evidence of the regional variations in microstructure (*i.e.*, coarse-grained and fine-grained regions).

ACKNOWLEDGMENTS

The authors thank Miaofang Chi, Javier E. Garay, and Yucheng Wang for insightful technical discussions and NCEM for the help on the high-resolution TEM. Financial support was provided by the Office of Naval Research (Grant No. N00014-03-C-0163).

APPENDIX

Material Property	Cryomilled Al
Atomic volume, Ω (m^3)	1.66×10^{-29}[46]
Burgers vector, b (m)	2.86×10^{-10}[46]
Melting temperature, T_m (K)	864
Yield strength at 300 K, σ_0 (MPa)	580[47]
Temperature dependence of strength, $\frac{T_m}{\sigma_0}\frac{d\sigma}{dT}$	−2.35[47]
Shear modulus at 300 K, μ_0 (GPa)	25.4[46]
Temperature dependence of modulus, $\frac{T_m}{\mu_0}\frac{d\mu}{dT}$	−0.50[46]
Lattice diffusion	
Pre-exponential, $D_{0\nu}$ (m^2/s)	1.7×10^{-4}[46]
Activation energy, Q_ν (kJ/mole)	142[46]
Boundary diffusion	
Pre-exponential, δD_{0b} (m^3/s)	5.0×10^{-14}[46]
Activation energy, Q_b (kJ/mole)	84[46]
Power-law creep	
Exponent, n	4.4[46]
Dorn constant, A	3.4×10^{6}[46]
Applied load, p (MPa)	80[46]
Radius of particle, R (μm)	15[46]
Initial relative density, D_0	0.63[46]

$\sigma_y = \sigma_0\left(1+\frac{(1-300)}{T_m}\right)\frac{T_m}{\sigma_0}\frac{d\sigma}{dT}; \mu = \mu_0\left(1+\frac{(1-300)}{T_m}\right)\frac{T_m}{\mu_0}\frac{d\mu}{dT}$; Ref. 41

$D_v = D_{0v}\exp\left(-\frac{Q_v}{RT}\right); \delta D_b = \delta D_{0b}\exp\left(-\frac{Q_b}{RT}\right)$; Ref. 41

$\frac{\dot{\varepsilon}}{\sigma_0^n} = \frac{AbD_v}{kT\mu^{n-1}}$; Ref. 41

$x = \frac{1}{\sqrt{3}}\left(\frac{D-D_0}{1-D_0}\right)^{1/2}R$; $\rho = R(D-D_0)$; $r = R\left(\frac{1-D}{6}\right)^{1/3}$; $P_{eff} = \frac{P(1-D_0)}{D^2(D-D_0)}$; Ref. 41

REFERENCES

1. H. Gleiter: *Acta Mater.*, 2000, vol. 48, pp. 1-29.
2. C. Suryanarayana: *Int. Mater. Rev.*, 1995, vol. 40, pp. 41-64.
3. D.G. Morris: *Mechanical Behavior of Nanostructured Materials,* Trans Tech Publications, Aedermannsdorf, Switzerland, 1998, pp. 1-18.
4. C. Suryanarayana: *Progr. Mater. Sci.*, 2001, vol. 46, pp. 1-184.
5. J. Ye and J.M. Schoenung: *Adv. Eng. Mater.*, 2004, vol. 6, pp. 656-64.
6. C.C. Koch: *Nanostruct. Mater.*, 1993, vol. 2, pp. 109-23.
7. F. Zhou, J. Lee, S. Dallek, and E.J. Lavernia: *J. Mater. Res.*, 2001, vol. 16, pp. 3451-8.
8. B.Q. Han, Z. Lee, S.R. Nutt, E.J. Lavernia, and F.A. Mohamed: *Metall. Mater. Trans. A*, 2003, vol. 34A, pp. 603-13.
9. J.A. Haber and W.E. Buhro: *J. Am. Chem. Soc.*, 1998, vol. 120, pp. 10847-55.
10. Y.S. Park, K.H. Chung, N.J. Kim, and E.J. Lavernia: *Mater. Sci. Eng., A*, 2004, vol. 374, pp. 211-26.
11. B.Q. Han, Z. Lee, D. Witkin, S. Nutt, and E.J. Lavernia: *Metall. Mater. Trans. A*, 2005, vol. 36A, pp. 1-9.
12. R. Chaim, Z. Shen, and M. Nygren: *J. Mater. Res.*, 2004, vol. 19, pp. 2527-31.
13. V. Mamedov: *Powder Metall.*, 2002, vol. 45, pp. 322-25.
14. J.E. Garay, U. Anselmi-Tamburini, and Z.A. Munir: *Acta Mater.*, 2003, vol. 51, pp. 4487-95.
15. J.E. Garay, S.C. Glade, U. Anselmi-Tamburini, P. Asoka-Kumar, and Z.A. Munir: *Appl. Phys. Lett.*, 2004, vol. 85, pp. 573-75.
16. M. Omori: *Mater. Sci. Eng., A*, 2000, vol. 287, pp. 183-88.
17. S.H. Risbud, J.R. Groza, and M.J. Kim: *Phil. Mag. B*, 1994, vol. 69, pp. 525-33.
18. G. Xie, O. Ohashi, T. Yoshioka, M. Song, K. Mitsuishi, H. Yasuda, K. Furuya, and T. Noda: *Mater. Trans.*, 2001, vol. 42, pp. 1846-49.
19. Y. Koizumi, T. Tanaka, Y. Minamino, N. Tsuji, K. Mizuuchi, and Y. Ohkanda: *Mater. Trans.*, 2003, vol. 44, pp. 1604-12.
20. H. Feng, Y. Zhou, D. Jia, and Q. Meng: *Mater. Sci. Eng., A*, 2005, vol. 390, pp. 344-49.
21. T. Murakami, A. Kitahara, Y. Koga, M. Kawahara, H. Inui, and M. Yamaguchi: *Mater. Sci. Eng., A*, 1997, vols. 239–240, pp. 672-79.
22. S. Paris, E. Gaffet, F. Bernard, and Z.A. Munir: *Scripta Mater.*, 2004, vol. 50, pp. 691-96.
23. Y. Minamino, Y. Koizumi, N. Tsuji, N. Hirohata, K. Mizuuchi, and Y. Ohkanda: *Sci. Technol. Adv. Mater.*, 2004, vol. 5, pp. 133-143.
24. S.H. Lee, K. Moon, H. Hong, and K. Lee: *Intermetallurgy*, 2003, vol. 11, pp. 1039-45.
25. M.A. Venkataswamy, J.A. Schneider, J.R. Groza, A.K. Mukherjee, K. Yamazaki, and K. Shoda: *Mater. Sci. Eng., A*, 1996, vol. 207, pp. 153-58.
26. M.S. El-Eskandarany: *J. Alloys Compounds*, 1998, vol. 279, pp. 263-71.
27. J. He, J. Ye, E.J. Lavernia, D. Matejczyk, C. Bampton, and J.M. Schoenung: *J. Mater. Sci.*, 2004, vol. 39, pp. 6957-64.
28. F.J. Humphreys and M. Hatherly: *Recrystallization and Related Annealing Phenomena*, Pergamon, Oxford, United Kingdom, 1996.
29. F. Zhou, X.Z. Liao, Y.T. Zhu, S. Dallek, and E.J. Lavernia: *Acta Mater.*, 2003, vol. 51, pp. 2777-91.
30. F. Tang, M. Hagiwara, and J.M. Schoenung: *Scripta Mater.*, 2005, vol. 53, pp. 619-24.
31. H.P. Klug and L.E. Alexander: *X-ray Diffraction Procedures for Polycrystalline and Amorphous Materials*, John Wiley & Sons, New York, NY, 1974, pp. 634-82.
32. L. Ajdelsztajn, R. Rodriguez, F.L. Bastian, and E.J.P. Lavernia: *Mater. Sci. Technol. Brief*, 2000, vol. 2, pp. 5-9.
33. W.F. Gale and T.C. Totemeier: *Smithells Metals Reference Book*, Elsevier Butterworth-Heinemann, Oxford, United Kingdom, 2004.
34. R.A. Vandermeer and H. Hu: *Acta Metall. Mater.*, 1994, vol. 42, pp. 3071-75.
35. G. Lormad, J.C. Rouais, and C. Eyraud: *Acta Metall.*, 1974, vol. 22, pp. 793-99.
36. S.M. Wentworth: *Fundamentals of Electromagnetics with Engineering Applications*, John Wiley, Hoboken, NJ, 2005, pp. 226-29.
37. T. Nakamura, S. Tanaka, K. Hayakawa, H. Imaizumi, and Y. Nakagawa: *Sosei to Kako*, 2003, vol. 44, pp. 931-36.
38. H. Hu: *Recovery and Recrystallization of Metals*, Interscience Publisher, New York, NY, 1963.
39. E.A. Olevsky, E.R. Strutt, and M.A. Meyers: *J. Mater. Proc. Technol.*, 2002, vol. 121, pp. 157-66.
40. E. Arzt, M.F. Ashby, and K.E. Easterling: *Metall. Trans. A*, 1983, vol. 14A, pp. 211-21.
41. A.S. Helle, K.E. Easterling, and M.F. Ashby: *Acta Metall.*, 1985, vol. 33, pp. 2163-74.
42. F.B. Swinkels, D.S. Wilkinson, E. Arzt, and M.F. Ashby: *Acta Metall.*, 1983, vol. 31, pp. 1829-40.
43. Y. Wang, Z. Fu, and Q. Zhang: *Key Eng. Mater.*, 2002, vols. 224–226, pp. 717-20.
44. Y. Wang and Z. Fu: *Mater. Sci. Eng., B*, 2002, vol. 90, pp. 34-37.
45. U. Anselmi-Tamburini, S. Gennari, J.E. Garay, and Z.A. Munir: *Mater. Sci. Eng., A*, 2005, vol. 394, pp. 139-48.
46. H.J. Frost and M.F. Ashby: *Deformation-Mechanism Maps the Plasticity and Creep of Metals and Ceramics*, Pergamon Press, New York, NY, 1982, p. 21.
47. B.Q. Han and E.J. Lavernia: *Mater. Sci. Eng. A*, 2005, vol. 410-411, pp. 417-21.